Coherent electrical control of a single high-spin nucleus in silicon

https://doi.org/10.1038/s41586-020-2057-7

Received: 10 June 2019

Accepted: 30 January 2020

Published online: 11 March 2020


Check for updates

Serwan Asaad[1,6], Vincent Mourik[1,6], Benjamin Joecker[1], Mark A. I. Johnson[1], Andrew D. Baczewski[2], Hannes R. Firgau[1], Mateusz T. Mądzik[1], Vivien Schmitt[1], Jarryd J. Pla[3], Fay E. Hudson[1], Kohei M. Itoh[4], Jeffrey C. McCallum[5], Andrew S. Dzurak[1], Arne Laucht[1] & Andrea Morello[1]✉

Nuclear spins are highly coherent quantum objects. In large ensembles, their control and detection via magnetic resonance is widely exploited, for example, in chemistry, medicine, materials science and mining. Nuclear spins also featured in early proposals for solid-state quantum computers[1] and demonstrations of quantum search[2] and factoring[3] algorithms. Scaling up such concepts requires controlling individual nuclei, which can be detected when coupled to an electron[4–6]. However, the need to address the nuclei via oscillating magnetic fields complicates their integration in multi-spin nanoscale devices, because the field cannot be localized or screened. Control via electric fields would resolve this problem, but previous methods[7–9] relied on transducing electric signals into magnetic fields via the electron–nuclear hyperfine interaction, which severely affects nuclear coherence. Here we demonstrate the coherent quantum control of a single ^{123}Sb (spin-7/2) nucleus using localized electric fields produced within a silicon nanoelectronic device. The method exploits an idea proposed in 1961[10] but not previously realized experimentally with a single nucleus. Our results are quantitatively supported by a microscopic theoretical model that reveals how the purely electrical modulation of the nuclear electric quadrupole interaction results in coherent nuclear spin transitions that are uniquely addressable owing to lattice strain. The spin dephasing time, 0.1 seconds, is orders of magnitude longer than those obtained by methods that require a coupled electron spin to achieve electrical driving. These results show that high-spin quadrupolar nuclei could be deployed as chaotic models, strain sensors and hybrid spin-mechanical quantum systems using all-electrical controls. Integrating electrically controllable nuclei with quantum dots[11,12] could pave the way to scalable, nuclear- and electron-spin-based quantum computers in silicon that operate without the need for oscillating magnetic fields.

Nuclear magnetic resonance (NMR) relies on the presence of a static magnetic field, B_0, that separates the energy levels of the nuclear spins, and a radio-frequency (RF) oscillating magnetic field, B_1, that induces transitions between such levels. Magnetic fields cannot be easily confined or screened at the nanoscale. Therefore, identical nuclear spins within large regions would all respond to the same signal, preventing the spins from being individually addressed. Electric fields, instead, can be efficiently routed and confined within highly complex nanoscale devices, with a prime example being the sophisticated interconnects found in modern silicon computer chips. These observations suggest that an ideal route to scale up nuclear-spin-based quantum devices would involve the use of RF electric fields for spin control.

A theoretical idea crucial to this strategy was proposed by Bloembergen as early as 1961[10]: for nuclei with spin $I > 1/2$ and non-zero electric quadrupole moment q_n, a resonant electric field induces nuclear spin transitions by modulating the nuclear quadrupole interaction, if the nuclei are placed in solids that lack point-inversion symmetry at the lattice site. In bulk ensembles, the static shift of the NMR frequency by a d.c. electric field, named linear quadrupole Stark effect (LQSE), was observed in the 1960s[13]. The resonant version of LQSE, called nuclear electric resonance (NER) was demonstrated only recently[14] in a bulk gallium arsenide (GaAs) crystal.

We report here the demonstration of NER and coherent electrical control of a single antimony (^{123}Sb) nucleus in silicon (Si). The discovery that this nucleus could be electrically controlled was fortuitous. The ^{123}Sb

[1]Centre for Quantum Computation and Communication Technology, School of Electrical Engineering and Telecommunications, UNSW Sydney, Sydney, New South Wales, Australia. [2]Center for Computing Research, Sandia National Laboratories, Albuquerque, NM, USA. [3]School of Electrical Engineering and Telecommunications, UNSW Sydney, Sydney, New South Wales, Australia. [4]School of Fundamental Science and Technology, Keio University, Yokohama, Japan. [5]Centre for Quantum Computation and Communication Technology, School of Physics, University of Melbourne, Melbourne, Victoria, Australia. [6]These authors contributed equally: Serwan Asaad, Vincent Mourik. ✉e-mail: a.morello@unsw.edu.au

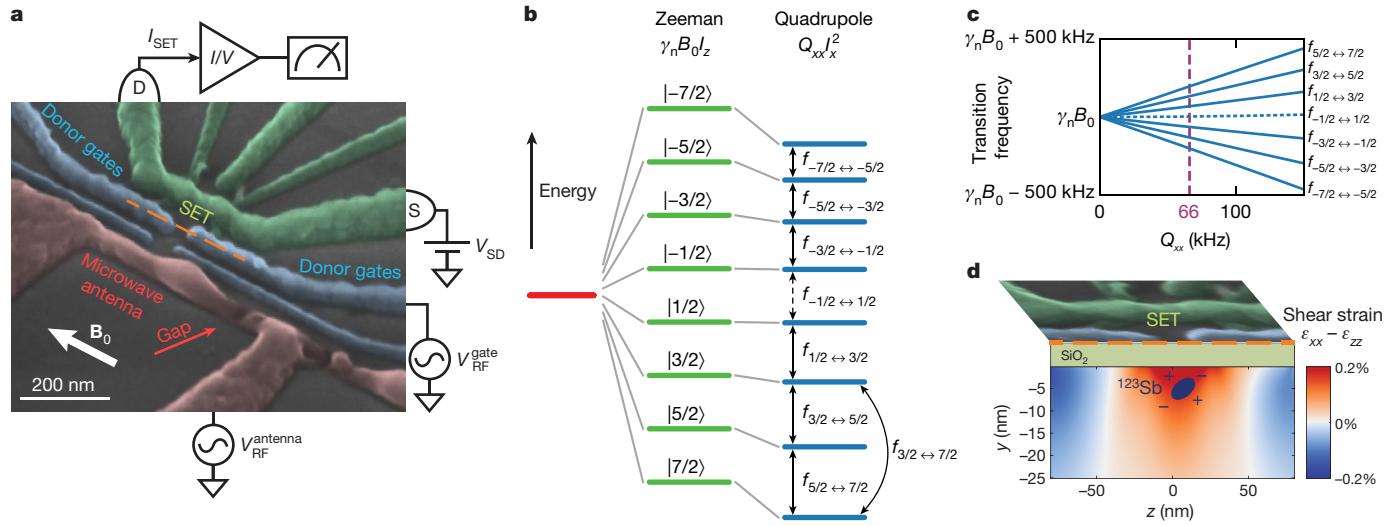

Fig. 1 | ^{123}Sb nuclear spin in a silicon device. a, False-colour scanning electron micrograph of the silicon metal–oxide–semiconductor device used in the experiment. Note the gaps in the nominally short-circuited antenna terminations. S, source; D, drain; SET, single-electron transistor. **b,** Energy-level diagram of the spin-7/2 nucleus of an ionized ^{123}Sb donor. The magnetic field B_0 introduces a Zeeman splitting (green dashes), and the electric quadrupole interaction Q_{xx} causes a further energy shift (blue dashes). **c**, Nuclear spin transition frequencies as a function of Q_{xx}. A non-zero Q_{xx} results in seven individually addressable nuclear resonances. The $m_I = -1/2 \leftrightarrow +1/2$ transition (dashed blue line in **c**) is forbidden in NER. The measured quadrupole splitting $f_Q = 66$ kHz is indicated by a dashed purple line. **d**, Shear strain in the silicon substrate, calculated on a vertical cross-section under the orange dashed line in **a**.

donor atom has a nuclear spin of $I = 7/2$ with electric quadrupole moment $q_n = -0.69$ b. Depending on its electrochemical potential relative to a nearby electron reservoir, an electron (with spin $S = 1/2$) may be bound to the nucleus. The atom was implanted in a metal–oxide–semiconductor nanostructure (Fig. 1a) fabricated on isotopically enriched ^{28}Si (for fabrication details, see Supplementary Information section 3), similar to those developed for phosphorus (^{31}P) spin qubits[5,15,16]. The structure contains a single-electron transistor (SET) for single-shot electron spin readout, which is based on energy-selective electron tunnelling into a cold charge reservoir[17]. Four electrostatic gates control the electrochemical potential of the donor, and a broadband on-chip microwave antenna[18] delivers coherent control signals to the donor spins. Single-shot, quantum non-demolition nuclear spin readout[5] is obtained by combining single-shot electron readout with selective excitation at a specific electron spin resonance frequency, which depends on the nuclear state because of the strong hyperfine interaction (see Methods). The antenna is nominally terminated by a short circuit, in order to obtain maximum current at its tip and produce strong oscillating magnetic fields to control both the electron (at about 40 GHz) and the nuclear (at about 10 MHz) spins of the donor. In this device, however, an electrostatic discharge damaged the short-circuit termination (Fig. 1a). Although the small gap in the termination had a low enough impedance at 40 GHz, to allow current flow for electron spin resonance, at about 10 MHz it produced solely an RF electric field. Once we realized that NER was possible, we began to use the electric gates fabricated exactly above the donor, which had an even stronger effect.

We focus here on the ^{123}Sb donor in its ionized state; the removal of the donor-bound electron precludes any interpretation of the data involving modulation of hyperfine fields[7,9]. The electron is introduced only for the final readout phase.

In nanoscale Si devices, the aluminium (Al) gates can cause considerable lattice strain at low temperatures, owing to the different thermal contraction of Al and Si (ref. [18]). Lattice strain creates an electric field gradient (EFG) of $\mathcal{V}_{\alpha\beta} = \partial^2 V/\partial\alpha\partial\beta$ (V is the electric potential and $\alpha, \beta \in \{x, y, z\}$) at the nuclear site[20,21] (Fig. 1b), which produces a static nuclear quadrupole interaction $Q_{\alpha\beta} = eq_n\mathcal{V}_{\alpha\beta}/[2I(2I-1)h]$ (h is the Planck constant and e is the electron charge), resulting in a quadrupole splitting f_Q of the nuclear resonance frequencies (Fig. 1d), making all transitions individually addressable.

The application of an RF electric field of amplitude E_1 modulates the nuclear quadrupole energies by δQ_{xz} and δQ_{yz}, and induces transitions between nuclear states at a rate of $f^{\mathrm{Rabi,NER}}_{m_I-1\leftrightarrow m_I} \propto |\delta Q_{xz}\langle m_I - 1|\hat{I}_x\hat{I}_z + \hat{I}_z\hat{I}_x|m_I\rangle|$, where m_I is the secondary spin quantum number, ranging from $-I$ to I in steps of 1, and $\hat{I}_x$, $\hat{I}_y$, $\hat{I}_z$ are the eight-dimensional operators describing the x, y, z projections of the $I = 7/2$ spin. Notably, the transition rate is predicted to be zero for the $m_I = -1/2 \leftrightarrow +1/2$ transition (see equation (15) in Supplementary Information section 2C), a consequence of the selection rules of electric quadrupole transitions. Because the quadrupole interaction is quadratic in the nuclear spin operators, first-order transitions between spin states that differ by $\Delta m_I = \pm 2$ are allowed. These occur at a rate of $f^{\mathrm{Rabi,NER}}_{m_I-2\leftrightarrow m_I} \propto |\delta Q_{xx}\langle m_I - 2|\hat{I}_x^2|m_I\rangle|$ (see equation (19) in Supplementary Information section 2C) and, importantly, all $\Delta m_I = \pm 2$ transitions have a non-zero rate.

Figure 2a shows the experimental NER spectrum for $\Delta m_I = \pm 1$ transitions, which contains six sharp resonances separated by $f_Q = 66$ kHz. The $m_I = -1/2 \leftrightarrow +1/2$ transition is absent, as expected from NER. All six predicted $\Delta m_I = \pm 2$ transitions are observed (Fig. 2b). The ability to excite the $m_I = -1/2 \leftrightarrow +3/2$ transition was used to 'jump over' the forbidden $m_I = -1/2 \leftrightarrow +1/2$ transition and observe the $\Delta m_I = \pm 1$ transitions at negative m_I, which would otherwise be inaccessible if starting from a positive m_I. Similarly, the NER spectrum for $\Delta m_I = \pm 2$ transitions (Fig. 2b) could be completed only by employing a $\Delta m_I = \pm 1$ transition.

Figure 2c, d presents the observed transition rates between each pair of states, in excellent agreement with the predicted trends from NER theory. Using NMR, the Rabi frequencies for the $\Delta m_I = \pm 1$ transitions would be $f^{\mathrm{Rabi,NMR}}_{m_I-1\leftrightarrow m_I} \propto |\gamma_n B_1\langle m_I - 1|\hat{I}_x|m_I\rangle|$ ($\gamma_n = 5.55$ MHz T^{-1} is the nuclear gyromagnetic ratio), which is notably maximal for the $m_I = -1/2 \leftrightarrow +1/2$ transition. The $\Delta m_I = \pm 2$ NMR transitions are forbidden to first-order. These results prove decisively that our experiments do not constitute a form of magnetic resonance.

As observed in earlier experiments on ^{31}P (refs. [16,22]), the nuclear spins of ionized donors in ^{28}Si have exceptional quantum coherence

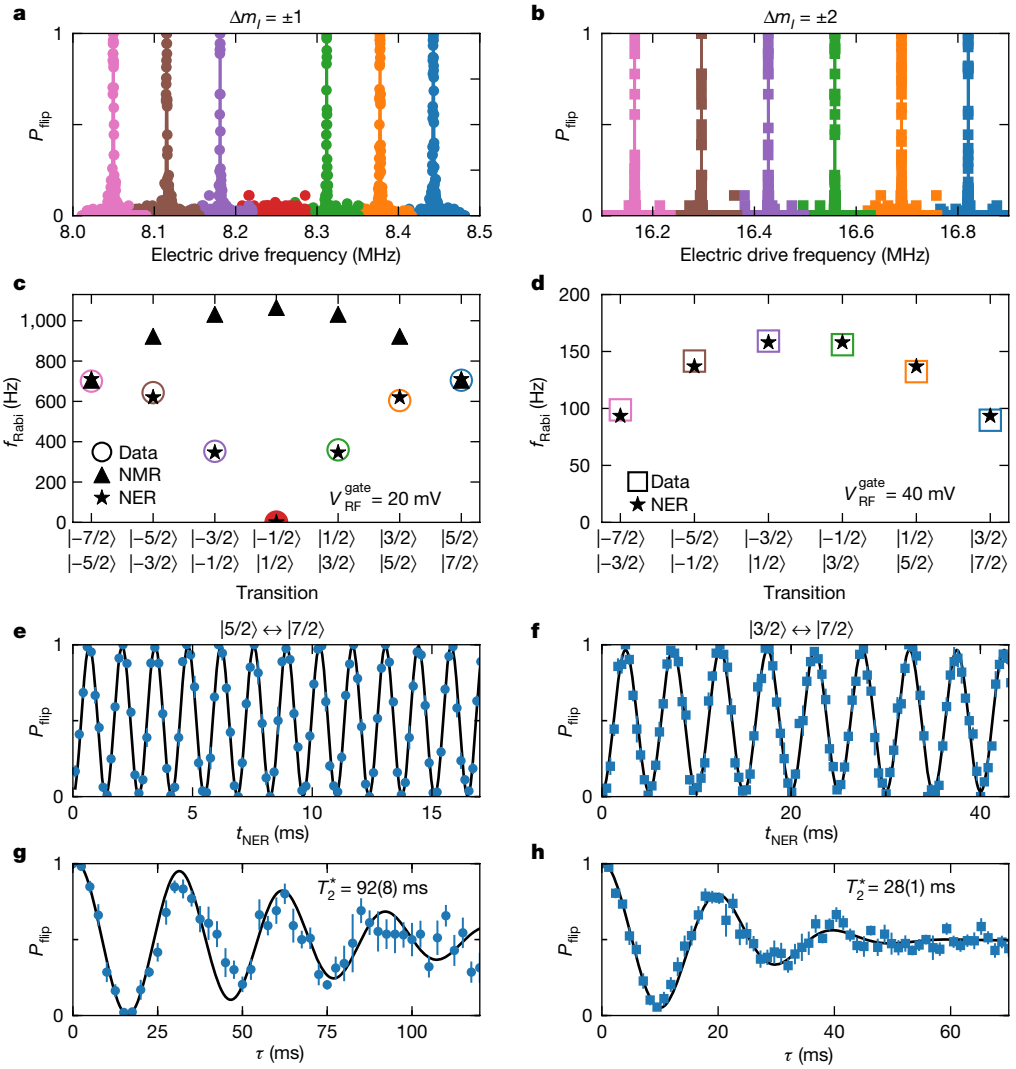

Fig. 2 | Nuclear electric resonance. **a**, **b**, NER spectrum for the $\Delta m_I = \pm 1$ (**a**) and $\Delta m_I = \pm 2$ (**b**) transitions, obtained by applying voltage V_{RF}^{gate} to a donor gate (see Fig. 1a). The $m_I = -1/2 \leftrightarrow +1/2$ transition (**a**, red) was not observed, as expected in NER. To acquire the complete $\Delta m_I = \pm 1$ spectrum, the $m_I = -1/2 \leftrightarrow +3/2$ transition was used to bridge the positive and negative m_I values. P_{flip} represents the probability of flipping the nuclear spin between two states. **c**, **d**, Rabi frequencies of the $\Delta m_I = \pm 1$ (**c**) and $\Delta m_I = \pm 2$ (**d**) transitions, each measured at a constant NER drive amplitude (see Extended Data Fig. 2 for the corresponding Rabi oscillations). Measured values (circles in **c**, squares in **d**) are compared to the theoretical predictions for NER (stars) and NMR (triangles in **c**), using the drive amplitude as the single free-scaling parameter to match the experimental values. All Rabi frequencies closely follow the NER prediction, including the absence of the $m_I = -1/2 \leftrightarrow +1/2$ transition (red circle in **c**, red dots in **a**), and are incompatible with NMR. **e**, **f**, Nuclear Rabi oscillations on the $m_I = +5/2 \leftrightarrow +7/2$ (**e**) and $m_I = +3/2 \leftrightarrow +7/2$ (**f**) transitions. A sinusoid with no decay is used to fit the data. t_{NER}, NER pulse duration. **g**, **h**, Nuclear Ramsey fringes used to extract the pure dephasing time T_{2n+}^* on the $m_I = +5/2 \leftrightarrow +7/2$ (**g**) and $m_I = +3/2 \leftrightarrow +7/2$ (**h**) transitions. The fits are sinusoids with envelopes decaying as $\exp[-(\tau/T_{2n+}^*)^2]$, where τ is the free precession time. Error bars and uncertainties denote the 68% confidence level.

properties. We performed a Ramsey experiment (Fig. 2g) on the $m_I = +5/2 \leftrightarrow +7/2$ ($\Delta m_I = \pm 1$) transition to extract the pure dephasing time $T_{2n+}^*(+5/2 \leftrightarrow +7/2) = 92(8)$ ms (68% confidence level), which corresponds to an NER broadening (full-width at half-maximum) of $\Gamma_n = \ln 2/(\pi T_{2n+}^*) = 2.4(2)$ Hz. The $m_I = +3/2 \leftrightarrow +7/2$ ($\Delta m_I = \pm 2$) transition has shorter dephasing time, $T_{2n+}^*(+3/2 \leftrightarrow +7/2) = 28(1)$ ms (Fig. 2h). Both values, although extremely long in absolute terms, are noticeably shorter than the time $T_{2n+}^* = 250$–600 ms measured on the ^{31}P nucleus in two other similar devices[16] fabricated on the same ^{28}Si wafer. Given that the ^{31}P nucleus has zero quadrupole moment, this suggests that the ^{123}Sb coherence may be affected by electrical noise[23], in a way that the ^{31}P coherence is not. Nonetheless, our dephasing time remains two orders of magnitude longer than that observed in ^{31}P when adding a hyperfine coupled electron, $T_{2n0}^* \approx 430$–570 μs (ref. [16]) and three orders of magnitude longer than the observed $T_2^* = 64$ μs of a terbium nucleus in a single-atom magnet[7]. This observation highlights the benefit of a purely electrical control mechanism that does not rely on hyperfine interactions.

We measured the Rabi frequencies of the $\Delta m_I = \pm 1$ and $\Delta m_I = \pm 2$ NER transitions as a function of the amplitude of the RF voltage applied to the gate, finding transition rates $g_{E,1} = 34.21(3)$ Hz mV^{-1} (Fig. 3a) and $g_{E,2} = 1.995(4)$ Hz mV^{-1} (Fig. 3b). These transition rates show that NER is a weak effect but, owing to the long nuclear spin coherence in ^{28}Si, we were able to perform high-fidelity Rabi flops persisting for tens of milliseconds (Fig. 2e, f).

In addition to driving nuclear spin transitions with an RF voltage, we were able to apply Stark shifts to the resonance frequencies using an additional d.c. voltage ΔV_{DC}^{gate} on the gates (Fig. 3c, d). All NER frequencies shifted according to $\Delta f = (\partial f_Q/\partial V_{DC}^{gate})|\Delta m_I|[m_I - (\Delta m_I/2)]\Delta V_{DC}^{gate}$, where $\partial f_Q/\partial V_{DC}^{gate} = 9.9(3)$ Hz mV^{-1}, and $|\Delta m_I|[m_I - (\Delta m_I/2)]$ is a factor of order unity that represents the matrix element of the electric quadrupole interaction between the initial and final state of each transition (see Supplementary Information section 2C for details).

The results reported here constitute the first, to our knowledge, observation of coherent, purely electrical control of a single nuclear spin. Achieving this in silicon is, at first sight, remarkable: no effect of electric fields on nuclear spins has ever been observed in a non-polar, non-piezoelectric material in the absence of a hyperfine-coupled electron. To gain a microscopic understanding of this phenomenon, we conjectured that our results are a form of LQSE[13]. Resonant transitions between nuclear levels induced by electric fields (NER) require that the crystal does not possess point-inversion symmetry at the atomic site[10], as is indeed the case for silicon. The observation of individual NER transitions, separated by the nuclear quadrupole splitting f_Q, implies that a static EFG must exist at the nuclear site. This requires breaking the T_d (tetrahedral) symmetry of the silicon crystal, as it would otherwise have zero net EFG. For instance, uniaxial strain (for example, ϵ_{zz}) lowers the symmetry to D_{2d} (tetragonal scalenohedral), whereas shear strain (for example, $\epsilon_{xx} - \epsilon_{zz}$) lowers it to C_{2v} (rhombic pyramidal). The T_d symmetry can also be broken by an electric field that polarizes the atomic bonds. This latter effect explains both the observation of NER and the static shift of the nuclear spin resonance lines (Fig. 3c, d) due to LQSE on application of a static gate voltage.

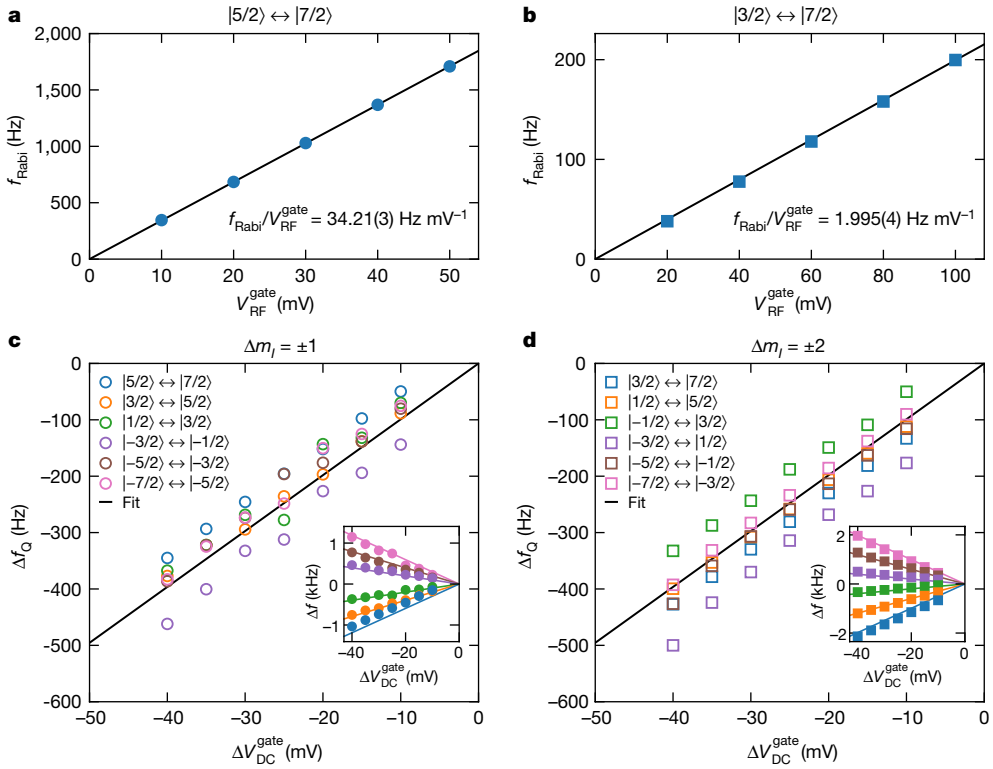

Fig. 3 | Linear quadrupole Stark effect. **a**, **b**, Rabi frequencies f_{Rabi} for varying electric drive peak amplitude V_{gate}^{RF}, measured on the $\Delta m_I = \pm 1$ transition $|5/2\rangle \leftrightarrow |7/2\rangle$ (**a**) and the $\Delta m_I = \pm 2$ transition $|3/2\rangle \leftrightarrow |7/2\rangle$ (**b**). The linear relationship between V_{RF}^{gate} and f_{Rabi} is consistent with a first-order transition induced by the LQSE. **c**, **d**, Quadrupole shift $\Delta f_Q = \left(\partial f_Q/\partial V_{DC}^{gate}\right)\Delta V_{DC}^{gate}$ measured while applying an additional d.c. voltage ΔV_{DC}^{gate} on a donor gate. The application of ΔV_{DC}^{gate} causes each transition frequency $f_{m_I-\Delta m_I \leftrightarrow m_I}$ to shift by $\Delta f = \left(\partial f_Q/\partial V_{DC}^{gate}\right)|\Delta m_I|[m_I - (\Delta m_I/2)]\Delta V_{DC}^{gate}$ (inset; see Extended Data Fig. 3 for nuclear spectra). A combined fit through all $\Delta m_I = \pm 1$ (**c**) and $\Delta m_I = \pm 2$ (**d**) frequency shifts results in an LQSE coefficient of $\partial f_Q/\partial V_{DC}^{gate} = 9.9(3)$ Hz mV^{-1}.

The larger and charged donor atom introduces a local lattice distortion, displacing its four coordinating Si atoms by 0.2 Å, and polarizes the charge density along the bonds (Fig. 4b, d). This, however, does not yet break the T_d symmetry. An EFG is obtained by further introducing strain. The S tensor that links EFG to strain has two unique components, S_{11} (uniaxial) and S_{44} (shear). We conducted a first-principles, density functional theory calculation and extracted $S_{11} = 2.4 \times 10^{22}$ V m^{-2} and $S_{44} = 6.1 \times 10^{22}$ V m^{-2} (see Supplementary Information section 7C2 for details). Using a finite-element numerical model we computed the strain profile in our device, as caused by the different thermal expansions of Si and Al on cooling to cryogenic temperatures[19,21] (Fig. 1b). Finally, we triangulated the most likely location of the ^{123}Sb donor by combining the implantation depth profile with a model of the relative capacitive coupling between the donor and different pairs of control gates, extracted from the experimental charge stability diagrams (see Extended Data Fig. 4 and Supplementary Information section 7C3 for details). By combining these three pieces of information, we arrived at a spatial map of quadrupole splittings f_Q (Fig. 4c), which shows good agreement between the models and the experiment around the predicted location of the donor under study.

The effect of electric fields on the quadrupole interaction, both static (LQSE) and dynamic (NER), can be understood as arising from the single unique component of the R tensor, R_{14} (see Supplementary Information section 7D1 for details). By combining a finite-element model of the electric field in the device, the estimated $^{123}Sb^+$ donor position and the experimental values of LQSE and NER Rabi frequencies, we extracted $R_{14} = 1.7 \times 10^{12}$ m^{-1} (see Supplementary Information section 7D2 for details). The strength of this coupling is comparable to prior bulk measurements of LQSE on arsenic (^{75}As) in GaAs (ref. [24]). This can be understood by observing that, although the Sb$^+$–Si bond has a weaker ionic character than the Ga–As bond, R_{14} scales with atomic number, leading to a similar overall value. Given that our model agrees with the experiment within a factor of order unity and no alternative explanation comes within orders of magnitude of the results (see Supplementary Information section 7E for details), we conclude that we have observed the manifestation of LQSE and NER in a single nuclear spin in silicon.

Our results have substantial consequences for the development of nuclear-spin-based quantum computers and the design of nanoscale quantum devices. The Hilbert space of the $I = 7/2$ ^{123}Sb nucleus has eight dimensions. It can encode the equivalent of three quantum bits of information, allowing simple quantum algorithms[25] or quantum error correction codes[26], all using solely electric fields. The donor electron and nuclear spins combined form a 'flip-flop' qubit[11], controllable by electric-dipole spin resonance. This scheme normally requires a magnetic antenna to reset the nuclear state in the appropriate qubit subspace. This need could be removed completely by using an electrically drivable high-spin nucleus such as ^{123}Sb. A recent result showed that lithographic quantum dots in silicon can be entangled with nuclear spins and that the nuclear coherence can be preserved while shuttling the electron between different dots[12]. Electron spin qubits in silicon can be coherently controlled by electric fields with high speed and high fidelity[27]. Adding the ability to electrically control quadrupolar nuclei paves the way to quantum computer architectures that integrate fast electron spin qubits with long-lived nuclear quantum memories while fully exploiting the controllability and scalability of silicon metal–oxide–semiconductor devices, without the complication of routing RF magnetic fields within the device.

The experimental validation of a microscopic model of the relation between strain and quadrupole splitting, obtained in a functional silicon electronic device, suggests the use of quadrupolar nuclei as single-atom probes of local strain, which has a key role in enhancing the performance of ultra-scaled transistors[28].

The NER methods and microscopic models presented here could be extended to the study of quadrupolar nuclei in materials such as diamond and silicon carbide, where electrical and strain tuning of optically addressable electronic spins has been demonstrated[29,30].

The observation of a large quadrupole splitting of $f_Q = 66$ kHz in a high-spin nucleus creates a platform in which to study quantum chaotic dynamics in a single particle[31]. This has further applications in quantum

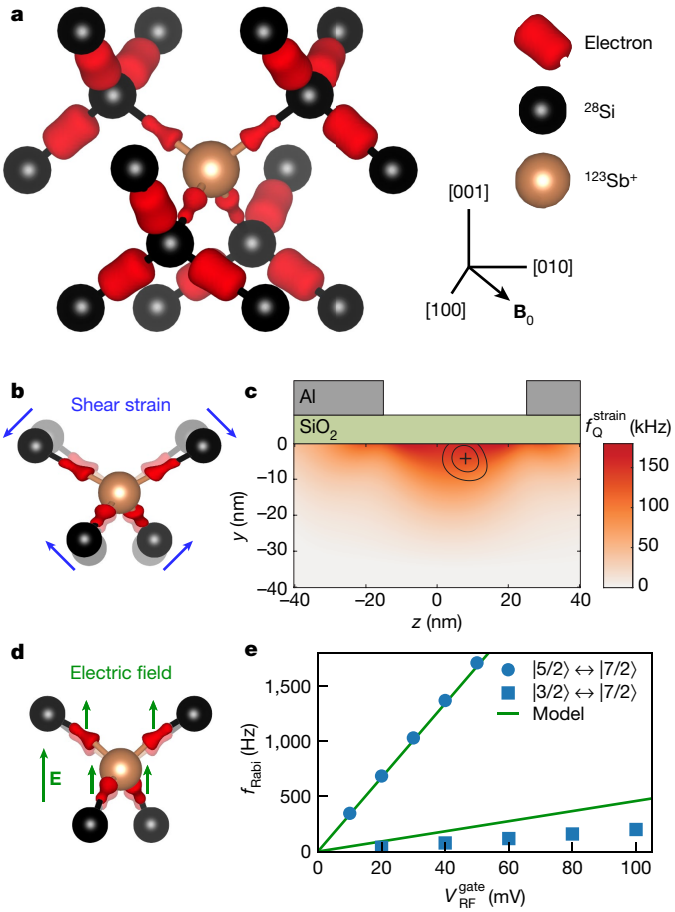

Fig. 4 | Microscopic origins of the quadrupole interaction. a, Valence charge density near the Sb^+ atom (gold) and its 16 closest Si atoms (black) with a charge density isosurface (red). The positive charge of the donor causes an asymmetric charge density along the Sb^+–Si bond but, in the absence of strain or external electric fields, the EFG at the ^{123}Sb site vanishes by symmetry. **b**, Shear strain displaces the Si atoms and covalent bonds neighbouring the ^{123}Sb nucleus, creating an EFG that results in a quadrupole shift. **c**, Quadrupole splitting f_Q, predicted by combining density functional theory calculations and finite-element simulations (see Supplementary Information section 7C for details). Black contours enclose the 68% and 95% confidence regions for the location of the donor, as obtained from capacitance triangulation and the donor implantation profile (see Supplementary Information section 7A for details). **d**, Electric fields applied via the gate voltage distort the charge distribution, resulting in both linear frequency shifts (LQSE) and coherent spin transitions (NER). **e**, Calculation of the NER Rabi frequencies caused by electrical EFG modulation (green lines), compared to experimental results for a $\Delta m_I = \pm 1$ (dots) and a $\Delta m_I = \pm 2$ (squares) transition. All f_{Rabi} values are determined using a single parameter, R_{14}, calculated via finite-element modelling and electronic structure theory. No free fitting parameters were used.

information science, for example, because of the remarkable analogies between chaotic spin models and digital quantum simulations[32].

Although the strain in the present device is static, our work allows us to predict the nuclear Rabi frequencies that would arise from time-dependent strain (see Supplementary Information section 8 for details). A dynamical strain of about 5×10^{-8} would cause a Rabi frequency of 10 Hz, comparable to both the inhomogeneous nuclear linewidth $\Gamma_n \approx 2.4$ Hz and to the linewidth Γ_n of high-quality silicon mechanical resonators in the megahertz range[33]. Therefore, it is conceivable that the strong-coupling limit of cavity quantum electrodynamics might be achieved between a single nuclear spin and a macroscopic mechanical oscillator, adding a novel spin–mechanical coupling pathway to the toolbox of hybrid quantum systems for quantum information processing and precision sensing[34].

Online content

Any methods, additional references, Nature Research reporting summaries, source data, extended data, supplementary information, acknowledgements, peer review information; details of author contributions and competing interests; and statements of data and code availability are available at https://doi.org/10.1038/s41586-020-2057-7.

1. Kane, B. E. A silicon-based nuclear spin quantum computer. *Nature* **393**, 133–137 (1998).
2. Jones, J. A., Mosca, M. & Hansen, R. H. Implementation of quantum search algorithm on a quantum computer. *Nature* **393**, 344–346 (1998).
3. Vandersypen, L. M. K. et al. Experimental realization of Shor's factoring algorithm using nuclear magnetic resonance. *Nature* **414**, 883–887 (2001).
4. Jelezko, F. et al. Observation of coherent oscillation of a single nuclear spin and realization of a two-qubit conditional quantum gate. *Phys. Rev. Lett.* **93**, 130501 (2004).
5. Pla, J. J. et al. High-fidelity readout and control of a nuclear spin qubit in silicon. *Nature* **496**, 334–338 (2013).
6. Willke, P. et al. Hyperfine interaction of individual atoms on a surface. *Science* **362**, 336–339 (2018).
7. Thiele, S. et al. Electrically driven nuclear spin resonance in single-molecule magnets. *Science* **344**, 1135–1138 (2014).
8. Laucht, A. et al. Electrically controlling single-spin qubits in a continuous microwave field. *Sci. Adv.* **1**, e1500022 (2015).
9. Sigillito, A. J., Tyryshkin, A. M., Schenkel, T., Houck, A. A. & Lyon, S. A. All-electric control of donor nuclear spin qubits in silicon. *Nat. Nanotechnol.* **12**, 958–962 (2017).
10. Bloembergen, N. Linear Stark effect in magnetic resonance spectra. *Science* **133**, 1363–1364 (1961).
11. Tosi, G. et al. Silicon quantum processor with robust long-distance qubit couplings. *Nat. Commun.* **8**, 450 (2017).
12. Hensen, B. et al. A silicon quantum-dot-coupled nuclear spin qubit. *Nat. Nanotechnol.* **15**, 13–17 (2020).
13. Dixon, R. & Bloembergen, N. Electrically induced perturbations of halogen nuclear quadrupole interactions in polycrystalline compounds. ii. Microscopic theory. *J. Chem. Phys.* **41**, 1739–1747 (1964).
14. Ono, M., Ishihara, J., Sato, G., Ohno, Y. & Ohno, H. Coherent manipulation of nuclear spins in semiconductors with an electric field. *Appl. Phys. Express* **6**, 033002 (2013).
15. Pla, J. J. et al. A single-atom electron spin qubit in silicon. *Nature* **489**, 541–545 (2012).
16. Muhonen, J. T. et al. Storing quantum information for 30 seconds in a nanoelectronic device. *Nat. Nanotechnol.* **9**, 986–991 (2014).
17. Morello, A. et al. Single-shot readout of an electron spin in silicon. *Nature* **467**, 687–691 (2010).
18. Dehollain, J. et al. Nanoscale broadband transmission lines for spin qubit control. *Nanotechnology* **24**, 015202 (2013).
19. Thorbeck, T. & Zimmerman, N. M. Formation of strain-induced quantum dots in gated semiconductor nanostructures. *AIP Adv.* **5**, 087107 (2015).
20. Franke, D. P. et al. Interaction of strain and nuclear spins in silicon: quadrupolar effects on ionized donors. *Phys. Rev. Lett.* **115**, 057601 (2015).
21. Pla, J. J. et al. Strain-induced spin-resonance shifts in silicon devices. *Phys. Rev. Appl.* **9**, 044014 (2018).
22. Saeedi, K. et al. Room-temperature quantum bit storage exceeding 39 minutes using ionized donors in silicon-28. *Science* **342**, 830–833 (2013).
23. Franke, D. P., Pflüger, M. P. D., Itoh, K. M. & Brandt, M. S. Multiple-quantum transitions and charge-induced decoherence of donor nuclear spins in silicon. *Phys. Rev. Lett.* **118**, 246401 (2017).
24. Gill, D. & Bloembergen, N. Linear Stark splitting of nuclear spin levels in GaAs. *Phys. Rev.* **129**, 2398–2403 (1963).
25. Godfrin, C. et al. Operating quantum states in single magnetic molecules: implementation of Grover's quantum algorithm. *Phys. Rev. Lett.* **119**, 187702 (2017).
26. Waldherr, G. et al. Quantum error correction in a solid-state hybrid spin register. *Nature* **506**, 204–207 (2014).
27. Yoneda, J. et al. A quantum-dot spin qubit with coherence limited by charge noise and fidelity higher than 99.9%. *Nat. Nanotechnol.* **13**, 102–106 (2018).
28. Thompson, S. E., Sun, G., Choi, Y. S. & Nishida, T. Uniaxial-process-induced strained-Si: extending the CMOS roadmap. *IEEE Trans. Electron Dev.* **53**, 1010–1020 (2006).
29. Dolde, F. et al. Electric-field sensing using single diamond spins. *Nat. Phys.* **7**, 459–463 (2011).
30. Falk, A. L. et al. Electrically and mechanically tunable electron spins in silicon carbide color centers. *Phys. Rev. Lett.* **112**, 187601 (2014).
31. Mourik, V. et al. Exploring quantum chaos with a single nuclear spin. *Phys. Rev. E* **98**, 042206 (2018).
32. Sieberer, L. M. et al. Digital quantum simulation, trotter errors, and quantum chaos of the kicked top. *npj Quantum Inf.* **5**, 78 (2019).
33. Ghaffari, S. et al. Quantum limit of quality factor in silicon micro and nano mechanical resonators. *Sci. Rep.* **3**, 3244 (2013); corrigendum 4, 4331 (2013).
34. Kurizki, G. et al. Quantum technologies with hybrid systems. *Proc. Natl Acad. Sci. USA* **112**, 3866–3873 (2015).

Methods

Fabrication

The device was fabricated on a ⟨100⟩ p-type silicon wafer, with a 900-nm-thick epitaxial layer of isotopically purified ^{28}Si on top (concentration of residual ^{29}Si, 730 ppm). Metallic leads for the SET were formed using optical lithography and phosphorus diffusion. The substrate was subsequently covered with a 200-nm-thick field oxide, with a small central window ($10 \times 20\ \mu m^2$) containing a high-quality, thermally grown layer of SiO_2 with a thickness of 8 nm. Using a combination of standard optical and electron-beam lithography techniques, the device was fabricated on this thin oxide window. First, a small ($90 \times 100\ nm^2$) window was defined, through which ^{123}Sb ions were implanted at an energy of 8 keV and a fluence of $2 \times 10^{11}\ cm^{-2}$, corresponding to an average of 14 donors in the implantation window. Donors were activated using a rapid thermal anneal at 1,000 °C for 5 s. Next, in two electron-beam lithography steps, the gates forming the SET, the donor gates and the microwave antenna were created using thermally evaporated aluminium and lift-off, with native aluminium oxide as the gate dielectric. Ohmic contacts to the n-doped SET leads were formed using optical lithography, evaporated Al and lift-off, followed by a forming gas anneal. A detailed step-by-step process flow is given in Supplementary Information section 3.

Experimental setup

The sample was cooled to a temperature of 20 mK in a dilution refrigerator (Bluefors BF-LD400) fitted with a superconducting magnet. During the measurements, arbitrary waveform generators (Signadyne M3201A and M3300A) were used to tune the donor electrochemical potential, generate NER pulses and IQ-modulate the microwave signals generated by a vector microwave source (Keysight E8267D). The SET current was amplified with a transimpedance amplifier (FEMTO DLPCA-200 in combination with Stanford Instruments SIM911) and subsequently measured with a digitizer (Signadyne M3300A). Full details of the experimental setup, including a wiring schematic, can be found in Supplementary Information section 4.

Nuclear spin readout

The nuclear spin state is measured via electron spin readout. For nuclear spin readout, an electron is introduced to the donor by tuning its electrochemical potential about the Fermi level of the SET such that a spin-down electron tunnels onto the donor. The electron spin resonance (ESR) spectrum (Extended Data Fig. 1) shows eight distinct resonance lines, each corresponding to a single nuclear spin eigenstate. The electron spin can be flipped conditionally on the nuclear spin state, resulting in single-shot nuclear spin readout. Electron spin readout is achieved by spin-to-charge conversion through spin-dependent tunnelling onto an SET and subsequent detection of the change in charge occupation of the donor (see Supplementary Information section 5 for details). As each of these electron spin measurements project the nucleus into a single spin eigenstate, this is a quantum non-demolition measurement. Therefore, each single-shot nuclear spin readout can be repeated to increase the nuclear spin readout fidelity while retaining the single-shot nature of the nuclear spin measurement. An NER pulse has a probability P_{flip} of flipping the nuclear spin between two states. To measure P_{flip}, an NER pulse followed by nuclear spin readout is performed $N_{\mathrm{iterations}}$ times. The first record of the nuclear spin state is used as a reference, and each subsequent record is compared to the one before it. This reveals the number of times that the nucleus flips, N_{flips}, between the two spin states. Therefore, the flip probability is simply the number of flips per number of recorded attempts, that is, $P_{\mathrm{flip}} = N_{\mathrm{flips}}/(N_{\mathrm{iterations}} - 1)$.

Theoretical modelling

The spin Hamiltonian of the ^{123}Sb nucleus takes the form:

$$\frac{\hat{H}}{h} = \gamma_n B_0 \hat{I}_z + \sum_{\alpha,\beta\in\{x,y,z\}} Q_{\alpha\beta}\hat{I}_\alpha\hat{I}_\beta \quad (1)$$

where $h = 6.626 \times 10^{-34}\ J\,Hz^{-1}$ is the Planck constant, $\gamma_n = -5.553\ MHz\ T^{-1}$ is the nuclear gyromagnetic ratio and $B_0 = 1.496$ T. In the presence of an RF electric field of amplitude E_1, the $\Delta m_I = \pm 1$ transitions are driven by an additional Hamiltonian term of the form:

$$\hat{H}^{\mathrm{NER}}_{m_I-1\leftrightarrow m_I}(t)/h = \cos(2\pi f t)[\delta Q_{xz}(\hat{I}_x\hat{I}_z + \hat{I}_z\hat{I}_x) + \delta Q_{yz}(\hat{I}_y\hat{I}_z + \hat{I}_z\hat{I}_y)] \quad (2)$$

The $\Delta m_I = \pm 2$ transitions are driven by a term of the form:

$$\hat{H}^{\mathrm{NER}}_{m_I-2\leftrightarrow m_I}(t)/h = \cos(2\pi f t)[\delta Q_{xx}\hat{I}_x^2 + \delta Q_{yy}\hat{I}_y^2 + \delta Q_{xy}(\hat{I}_x\hat{I}_y + \hat{I}_y\hat{I}_x)] \quad (3)$$

A detailed derivation of the matrix elements responsible for driving the $\Delta m_I = \pm 1$ and $\Delta m_I = \pm 2$ NER transitions is given in Supplementary Information section 2C. A finite-element model is used to compute the strain and electric fields in the silicon layer near the donor position using the COMSOL multiphysics software. The donor position is triangulated by comparing simulated gate-to-donor coupling strengths with the experimentally observed strength, combined with the donor implantation profile (see Extended Data Fig. 4 and Supplementary Information section 7A). Kohn–Sham density functional theory is employed to calculate the components of the S tensor that describe the impact of strain on the EFG. To this end, 64- and 512-atom supercells were strained using the PAW (projector augmented-wave) formalism[35] with a plane-wave basis, as implemented in VASP (Vienna ab initio simulation package)[36–38]. The electric-field response tensor is estimated by comparing the data points from the d.c. LQSE (Fig. 3c, d) and $\Delta m_I = \pm 1$ (Fig. 2c) and $\Delta m_I = \pm 2$ (Fig. 2d) Rabi frequencies with the simulated electric fields at the triangulated donor position. The final R_{14} is found by minimizing the normalized residuals of the three separate R_{14} estimates. Full theoretical modelling details can be found in Supplementary Information section 7.

Data availability

All data necessary to evaluate the claims of this paper are provided in the main manuscript and Supplementary Information. Raw data files, data analysis code and simulation code are available at https://doi.org/10.26190/5de9c295a8821.

35. Blöchl, P. E. Projector augmented-wave method. *Phys. Rev. B* **50**, 17953–17979 (1994).
36. Kresse, G. & Furthmüller, J. Efficient iterative schemes for ab initio total-energy calculations using a plane-wave basis set. *Phys. Rev. B* **54**, 11169–11186 (1996).
37. Kresse, G. & Furthmüller, J. Efficiency of ab initio total energy calculations for metals and semiconductors using a plane-wave basis set. *Comput. Mater. Sci*. **6**, 15–50 (1996).
38. Kresse, G. & Joubert, D. From ultrasoft pseudopotentials to the projector augmented-wave method. *Phys. Rev. B* **59**, 1758–1775 (1999).
39. Mansir, J. et al. Linear hyperfine tuning of donor spins in silicon using hydrostatic strain. *Phys. Rev. Lett*. **120**, 167701 (2018).

Acknowledgements We thank T. Botzem and J. T. Muhonen for discussions. The research was funded by the Australian Research Council Discovery Projects (grants DP150101863 and DP180100969) and the Australian Department of Industry, Innovation and Science (grant AUSMURI00002). V.M. acknowledges support from a Niels Stensen Fellowship. M.A.I.J. and H.R.F. acknowledge the support of Australian Government Research Training Program Scholarships. J.J.P. is supported by an Australian Research Council Discovery Early Career Research Award (DE190101397). A.M. was supported by a Weston Visiting Professorship at the Weizmann Institute of Science during part of the writing of this manuscript. We acknowledge support from the Australian National Fabrication Facility (ANFF), and from the laboratory of R. Elliman at the Australian National University for the ion implantation facilities. A.D.B. was supported by the Laboratory Directed Research and Development programme at Sandia National Laboratories, Project 213048. Sandia National Laboratories is a multi-missions laboratory managed and operated by National Technology and Engineering Solutions of Sandia, LLC, a wholly owned subsidiary of Honeywell International Inc., for the National Nuclear Security Administration of the US Department of Energy under contract DE-NA0003525. The views expressed in this manuscript do not necessarily represent the views of the US Department of Energy or the US Government. K.M.I. acknowledges support from Grant-in-Aid for Scientific Research by MEXT.

Author contributions S.A. and M.A.I.J. performed the measurements under the supervision of V.M., A.L. and A.M., with the assistance of V.S., M.T.M. and H.R.F.; S.A. and M.A.I.J. analysed the data under the supervision of V.M. and A.M., with the assistance of H.R.F., V.S., J.J.P. and A.L.; A.D.B., S.A., V.M., B.J. and A.M. developed a microscopic theory supported by finite-element modelling by B.J. and electronic structure calculations by A.D.B.; F.E.H. partially fabricated the device under the supervision of A.S.D., on isotopically enriched material supplied by K.M.I. and M.T.M. subsequently fabricated the aluminium gate structures under the supervision of V.M. and A.M.; J.C.M. designed and performed the ^{123}Sb ion implantation; S.A., V.M., B.J., M.A.I.J., A.D.B., H.R.F. and A.M. wrote the manuscript and Supplementary Information, with input from all co-authors; A.M. initiated and supervised the research programme.

Competing interests S.A., V.M. and A.M. have submitted a patent application that describes the use of electrically controlled high-spin nuclei for quantum information processing (AU2018900665A).

Additional information

Supplementary information is available for this paper at https://doi.org/10.1038/s41586-020-2057-7.

Correspondence and requests for materials should be addressed to A.M.

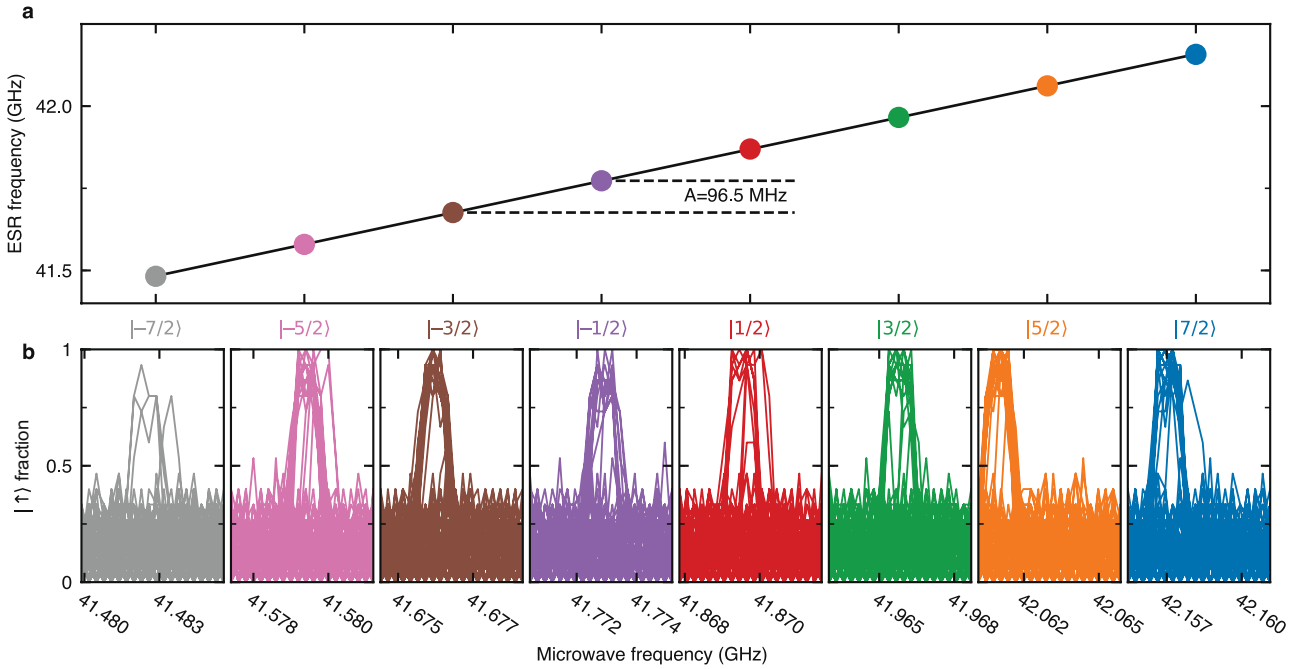

Extended Data Fig. 1 | ESR spectrum in a magnetic field of B_0 = 1.496 T. a, ESR frequencies for eight nuclear states. The average difference between successive ESR transition frequencies (black line) gives a hyperfine interaction of A = 96.5 MHz, substantially lower than the bulk value of 101.52 MHz. One possible cause for this deviation is strain, which is known to modify the hyperfine interaction[39]. **b**, ESR spectral lines. For each nuclear state, the nucleus was initialized at the start of each microwave sweep, and adiabatic ESR pulses with 1 MHz frequency deviation were applied to excite the electron.

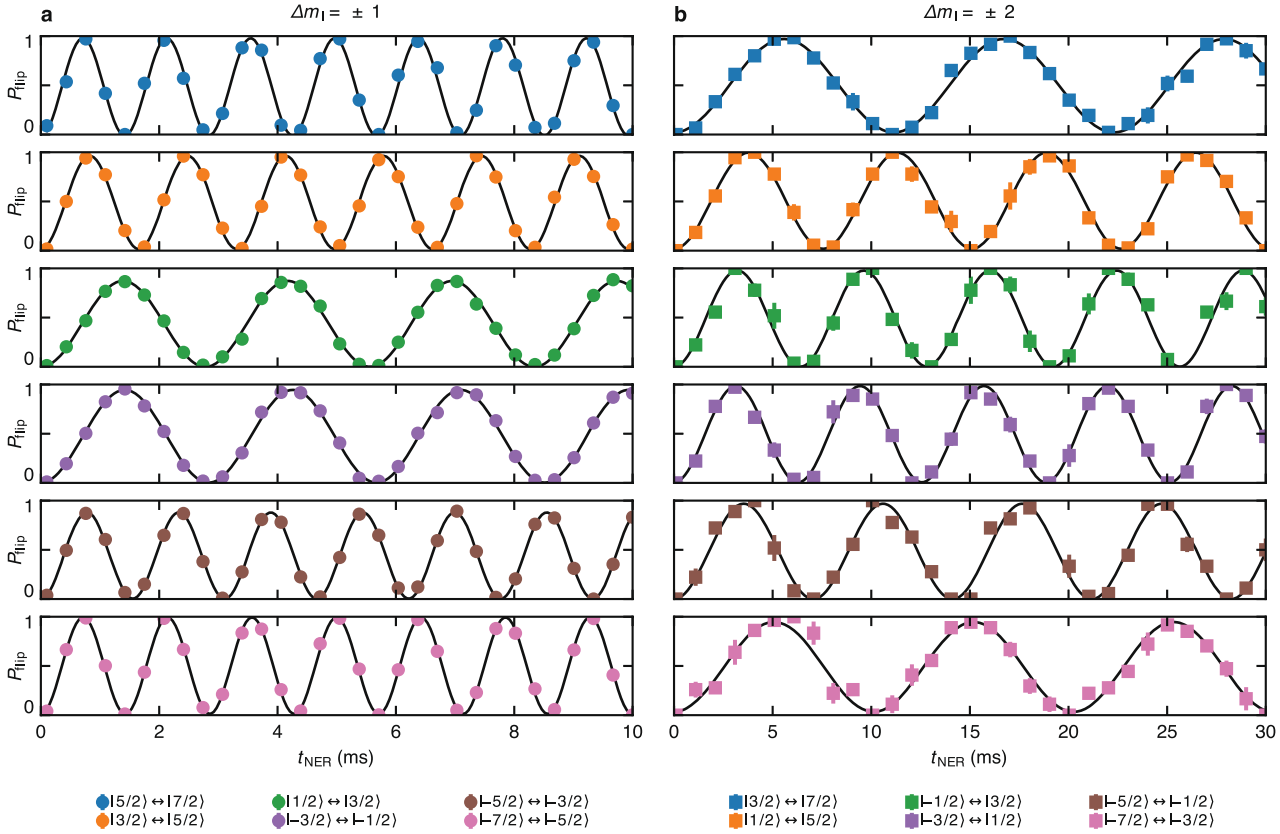

Extended Data Fig. 2 | NER Rabi oscillations on resonance. a, **b**, Nuclear Rabi oscillations measured with varying NER pulse duration, t_{NER}, while the pulse amplitude was fixed at $V_{\mathrm{gate}}^{\mathrm{RF}} = 20$ mV for $\Delta m_I = \pm 1$ transitions (**a**) and $V_{\mathrm{gate}}^{\mathrm{RF}} = 40$ mV for $\Delta m_I = \pm 2$ transitions (**b**). Black lines are non-decaying sinusoidal fits to the data, and error bars show the 68% confidence level.

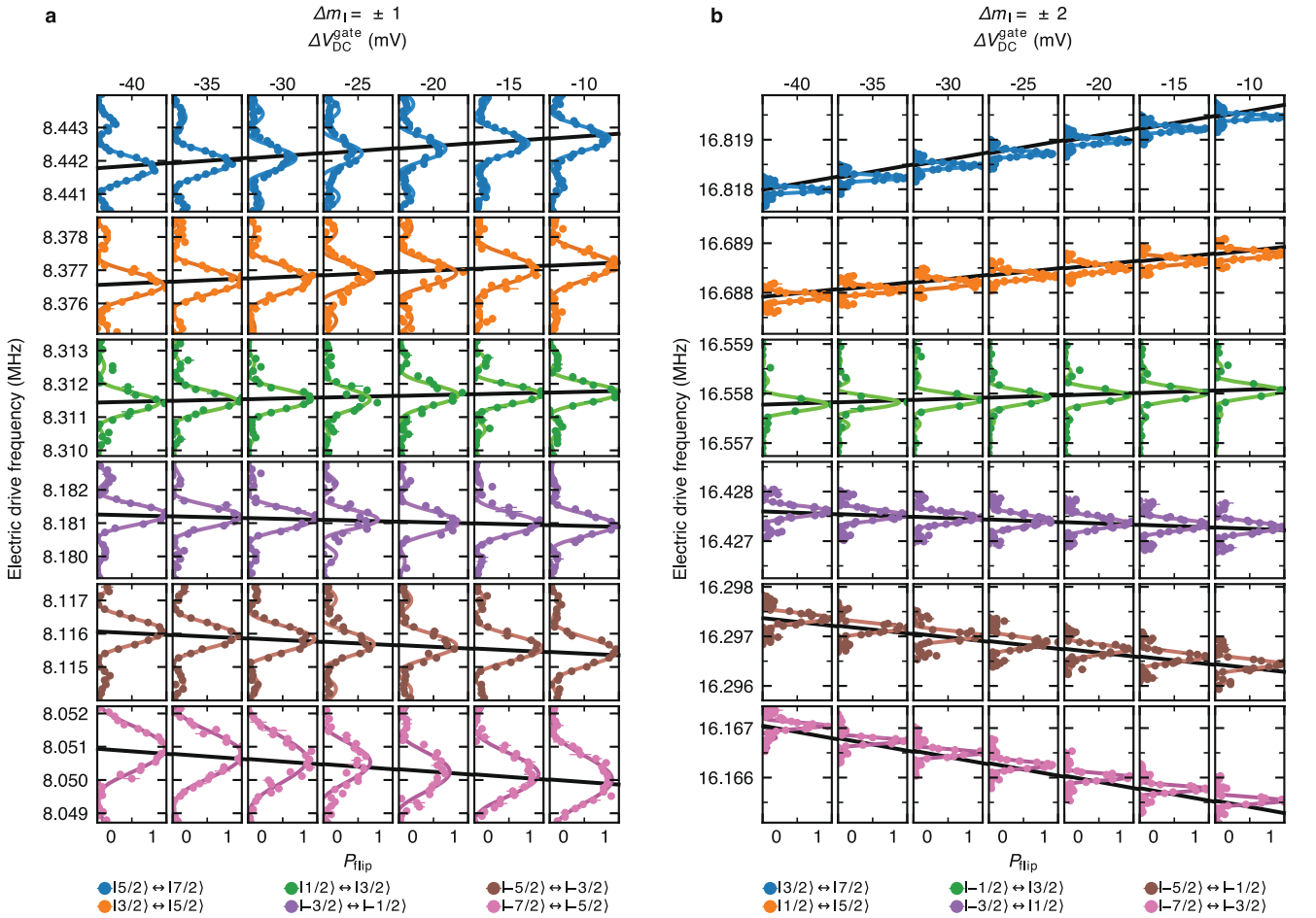

Extended Data Fig. 3 | NER spectral line shifts for varying d.c. gate voltage. **a**, **b**, The spectral lines of all $\Delta m_I = \pm 1$ transitions (**a**) and $\Delta m_I = \pm 2$ (**b**) transitions are measured while the d.c. gate voltage bias ΔV_{DC}^{gate} is varied (columns) during the NER pulse. We note that this change in V_{DC}^{gate} is applied on top of large gate voltages, of the order of 0.5 V, which are necessary to electrostatically tune the device to enable its operation. The varying ΔV_{DC}^{gate} modifies the quadrupole interaction via the LQSE (see Supplementary Information section 7 for details), resulting in shifts of the resonance peaks. A single fit to the resonance frequency shifts of all $\Delta m_I = \pm 1$ and $\Delta m_I = \pm 2$ transitions (solid lines) gives an estimate of the gate-dependent quadrupole shift of $\partial f_Q / \partial V_{DC}^{gate} = 9.9(3)$ Hz mV^{-1}. From the top to the bottom transition, the drive strengths V_{RF}^{gate} are 20 mV, 20 mV, 25 mV, 25 mV, 20 mV and 25 mV for $\Delta m_I = \pm 1$ (**a**) and 30 mV, 30 mV, 40 mV, 40 mV, 40 mV and 40 mV for $\Delta m_I = \pm 2$ (**b**). Error bars show the 68% confidence level.

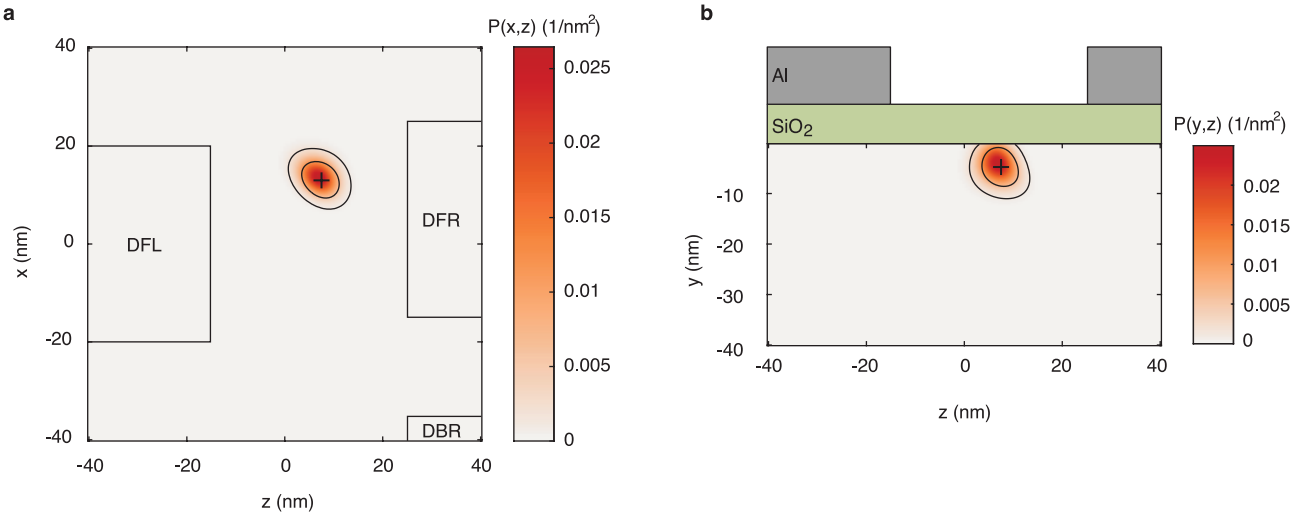

Extended Data Fig. 4 | Position triangulation of the ^{123}Sb donor. The colour map shows the probability of finding the donor in a certain location. **a**, **b**, Probability density function found using a least-squares estimation comparing simulated gate-to-donor coupling strengths with the experimentally observed strengths (see Supplementary Information section 7A for details, including the locations of the donor gates DFR, DFL and DBR). To improve on the low resolving power of the triangulation method in the *y* direction, the triangulation probability density function is multiplied with the donor implantation probability density function (see Supplementary Information section 7A for details). This has little effect laterally, but greatly confines the likely depth range of the donor within the range expected on the basis of the donor implantation parameters. The most likely donor position, indicated by a cross, is at the lateral location $(x, z) = (13\ \text{nm}, 8\ \text{nm})$ at a depth of $y = -5$ nm. The probability density functions are normalized over the model volume and are integrated over the out-of-plane axis in both panels, specifically, $P(x,z) = \int P(\mathbf{r})\mathrm{d}y$ and $P(y,z) = \int P(\mathbf{r})\mathrm{d}x$. The contour lines mark the 68% and 95% confidence regions.